Supplementary Information: Molecular mechanisms and energetics of lipid droplet formation and directional budding

Fatemeh Kazemisabet,[†] Arash Bahrami,[†] Rikhia Ghosh,[‡] Bartosz Różycki,[¶] and Amir H. Bahrami[*,§,‖]

†*School of Mechanical Engineering, College of Engineering, University of Tehran, North Kargar St., 14399-57131 Tehran, Iran*

‡*Department of Pharmacological Sciences, Icahn School of Medicine, Mount Sinai, New York 10029, United States*

¶*Institute of Physics, Polish Academy of Sciences, Al. Lotników 32/46, 02-668 Warsaw, Poland*

§*Living Matter Physics, Max Planck Institute for Dynamics and Self-Organization, 37077 Göttingen, Germany*

‖*Living Matter and Biophysics, UNAM-National Nanotechnology Research Center and Institute of Materials Science & Nanotechnology, Bilkent University, Ankara, Turkey*

E-mail: bahrami@unam.bilkent.edu.tr

Supplementary Text

S1. Assembling initial slabs

We started by assembling initial slabs, wherein a given volume V of oil is covered by two flat lipid monolayers from below and above with their hydrophobic chains facing the oil, see Fig. 1a and supplementary Fig. S1b. Initial monolayers were assembled by placing different number of lipids N_{lip}, equally divided between two monolayers of fixed width L in a cubic simulation box with periodic boundary conditions. Each slab with a given number of lipids N_{lip} has then a fixed projected area-per-lipid $A_{lp} = 2A_s/N_{lip}$, defined as the average area-per-lipid projected into the horizontal plane.

S2. Shape parameters of LDs

We first computed the thickness of the ER-bilayer $l_b = 4.08\ nm$ as the distance between the peaks of the density of lipid head groups of a flat bilayer, see supplementary Fig. S1a. The monolayer thickness was then taken to be $l_m = 0.5 l_b = 2.04\ nm$. We assumed that LD-monolayers of all LDs, obtained from DPD simulations, have the shape of spherical caps to minimize membrane bending cost for a given membrane surface area. To find the shape of symmetrical LD lenses and spherical LDs, we fitted spherical caps to the simulation results and computed their shape parameters according to Figure 2a. Complete spheres of size $R = 0.5D$ were fitted to the asymmetric budding LDs. The contact point of the ER-bilayer with these spheres were then used to find the LD angles as shown in the right panel of Fig. 5b. The spherical caps of symmetrical LDs were parametrized by the radius of the sphere and the Cartesian coordinates x_s, y_s, and z_s of its center. The sum S of the mean square distances of all beads i of LD lipids from the surface of the cap

$$S = \sum_i \left(\sqrt{(x_i - x_s)^2 + (y_i - y_s)^2 + (z_i - z_s)^2} - R \right)^2 \qquad \text{(S1)}$$

was then minimized by setting the derivatives

$$\partial S/\partial x_s = \partial S/\partial y_s = \partial S/\partial z_s = \partial S/\partial R = 0 \tag{S2}$$

leading to a system of four equations from which the radius R of the cap and the Cartesian coordinates of the cap center were obtained. The contact angle was then computed from the fitted cap. In this way, we fitted spherical caps to LD-monolayers and obtained the radii and lens angles of the luminal and cytosolic LD-monolayers for different LD shapes.

S3. Membrane tension and bending stiffness

To find membrane properties such as membrane thickness and bending stiffness of bilayers and monolayers, we simulated small flat bilayers and small slabs. The slabs were simulated in a cubic box of fixed width 25.6 nm and initial height 25.6 nm with $N_{oil} = 10,363$ oil molecules surrounded by 35,852 water beads forming slabs of size $D = 24.2\ nm$, see Fig. 1a. The number of lipids N_{lip}, equally partitioned between the two slab monolayers, was varied to generate slabs with different A_{lp}, see supplementary Table S2. Flat bilayers were also simulated in cubic boxes of the same size with the same N_{lip} and thus the same A_{lp} as the slabs, see the snapshot in supplementary Fig. S2c and the data in supplementary Table S2.

Both slabs and flat bilayers were first equilibrated for 2 μs in an NPT ensemble using a Berendsen barostat in the vertical direction z, see supplementary Fig. S2a,c, adjusting the pressure at 23.7 $k_BT/d^3 = 190.4 \times 10^9\ mN/m^2$. During NPT simulations the height of the simulation boxes changed to adjust the pressure while their widths remained constant at 25.6 nm. We note that the density of the simulation box, including both water and oil, slightly varies during NPT simulations but the water density remains at $5.86/nm^3$ as shown in the density plots in the bottom panels of Fig. S1. Membrane tensions were then computed in following 22 μs-long runs in an NVT ensemble with fixed simulation boxes at room temperature. We used the integral

$$\Sigma = \int_{-h}^{h} s(z)dz = \int_{-h}^{h} [P_N(z) - P_T(z)]dz \tag{S3}$$

of the stress profile $s(z) = P_N(z) - P_T(z)$ to find both monolayer and bilayer tensions, Σ_m and Σ_b, respectively. Here, P_N and P_T denote normal and tangential pressure components, computed across an almost planar patch of a bilayer or a monolayer membrane in the z direction perpendicular to the membrane surface.[1,2] We first calculated membrane tensions inside small slabs of size $D = 24.2$ nm to demonstrate that monolayer tensions increase linearly with A_{lp}. The Cartesian coordinate system was placed in the center of the slabs and the stress profile was computed inside a box of width 13 nm and height $2h = 20$ nm, see supplementary Fig. S2a. The monolayer tensions were then calculated as

$$\begin{aligned} \Sigma_{lm} &= \int_{0}^{h} s(z)dz = \int_{0}^{h} [P_N(z) - P_T(z)]dz \\ \Sigma_{cm} &= \int_{0}^{-h} s(z)dz = \int_{0}^{-h} [P_N(z) - P_T(z)]dz \end{aligned} \tag{S4}$$

The monolayer tension $\Sigma_m = 0.5(\Sigma_{lm} + \Sigma_{cm})$ was taken to be the average of almost equal tensions in the outer (cytosolic) and inner (luminal) monolayers. Supplementary Figure S2b shows the stress profiles of some of these small slabs with corresponding Σ_m's and A_{lp}'s whose values are listed in supplementary Table S2.

We computed the monolayer tension Σ_m in the initial flat monolayers of three small slabs of size $D = 24.2$ nm and area $A_s = 655.4$ nm^2, with different A_{lp}'s, see Fig. 1b. The slab area was chosen to be smaller than $A_{sm} = 1115.3$ nm^2 for $L = 25.6$ nm to prevent the slab-to-lens transition. The monolayer tension increased from 0.4 mN/m for $A_{lp} = 0.72$ nm^2 to 10.5 mN/m for $A_{lp} = 0.82$ nm^2 corresponding to monolayers with $N_{lip} = 1800$ and $N_{lip} = 1600$ lipids, respectively, see supplementary Fig. S2b and Table S2. We thus verified that lipid membranes with larger A_{lp}'s experience larger membrane tensions.

We then used equation (S3) to obtain stress profiles of flat bilayers in a box of width

13 nm and initial height $h = 5\ nm$, see supplementary Fig. S2c. Supplementary Figure S2d shows the resulting stress profiles across two flat bilayers. For both bilayers and monolayers (slabs), membrane tensions and areas-per-lipid were averaged over 400 simulation frames. These simulations were performed for 20 μs in an NVT ensemble during which 400 equally distanced frames were picked to compute the average Σ's and A_{lp}'s as listed in supplementary Table S2. These tensions, plotted against the corresponding A_{lp} values by blue and red dots in supplementary Fig. S2e, were then used to compute the bending rigidities of the ER-bilayer and LD-monolayers.

We fitted a line to the data of Σ_m versus A_{lp}, and found $A^m_{l0} = 0.715\ nm^2$ corresponding to zero tension $\Sigma_m = 0$. The area extension elastic modulus was then obtained as the product $K^m_A = A^m_{l0}(d\Sigma_m/dA^m_l) = 68.3\ pN/nm$, where $d\Sigma_m/dA^m_l = 95.6\ pN/nm^3$.[3] The bending rigidity of the monolayer was then found as $\kappa_m = (1/12)K^m_A l^2_m = 23.7\ pN \cdot nm$, where $l_m = 2.04\ nm$ is the monolayer thickness i.e. half the bilayer thickness $l_m = 0.5 l_b$. A similar procedure was used to find the bending rigidity of the ER-bilayer as:

$$
\begin{aligned}
d\Sigma_b/dA^b_l &= 215.3\ pN/nm^3 \\
A^b_{l0} &= 0.778\ nm^2 \\
K^b_A &= A^b_{l0}(d\Sigma_b/dA^b_l) = 167.5\ pN/nm \\
\kappa_b &= (1/48)K^b_A l^2_b = 58.1\ pN \cdot nm
\end{aligned}
\tag{S5}
$$

In this way, we found the bending rigidities, $\kappa_b = 58.1\ pN \cdot nm$ and $\kappa_m = 23.7\ pN \cdot nm$, of the ER-bilayer and LD-monolayers, respectively.

S4. LD parameters

Spontaneous formation of LDs from initial oil slabs were simulated in a fixed simulation box of size $(48 \times 48 \times 72)\ nm^3$ composed of N_{lip} lipids placed in two monolayers exposed to water from above and below with a fixed total of 972000 beads. The number of lipids was then varied, as listed in supplementary Table S3, to change the projected area-per-lipid A_{lp} for different LD sizes $D = 29.5$, 31, and 33.2 nm as seen in the morphological diagram in Fig. 1c. Spontaneous formation of different LD structures occurred in 5 μs in an NPT ensemble at constant pressure $190.4 \times 10^9\ mN/m^2$, using a Berendsen barostat in the vertical direction z perpendicular to the slab monolayers. The initial slabs transformed to a variety of LD structures as shown in Fig. 1c.

S5. The transition of LD lenses to spherical LDs

We performed the transition simulations starting from an almost spherical LD of size $D = 29.5\ nm$ with the largest lens angle $\theta = 86°$, spontaneously formed from an initial slab with $N_{oil} = 21,000$ and $N_{lip} = 6960$. We then increased the width L of the simulation box in an NPT ensemble with a barostat in the vertical direction z perpendicular to the ER-bilayer for a constant number of lipids and water beads.

We increased the width of the simulation box at a rate 0.4 pm/ns resulting in a quasi-equilibrium transition with intermediate equilibrium LD lenses.[4] The procedure was then repeated successively to find different lenses shown in Fig. 2b. After reaching the target box width for each lens angle, we continued the simulation for 8 μs, this time in the NVT ensemble, the last 6 μs of which was used to compute membrane tensions by averaging over 120 frames, and A_l values, and LD shape parameters by averaging over 12 frames. LD-tensions were computed, using the equations (S4), in a box of width 8 nm and height 48 nm, which contained almost flat monolayer patches as shown in supplementary Fig. S4. ER-tensions were computed using equation (S3) inside a box of size $(8 \times 48 \times 48)\ nm^3$, see supplementary Fig. S4. The same boxes were used to compute A_l values for both the ER-bilayers and LD-monolayers. Supplementary Table S4 lists the LD parameters for the resulting seven LDs shown in Fig. 2b. To compare different LD sizes, we also performed the transition simulations for another LD of size $D = 27.7\ nm$ with $N_{oil} = 16800$ and $N_{lip} = 6800$, the parameters of which are presented in supplementary Table S5. See the supplementary text for details on line tension calculation during LD transition.

S6. Line tensions in symmetrical LDs

The free energy of a symmetrical LD with the surrounding ER-bilayer is given by

$$F_s = 2E_{bs} + A_{bs}\Sigma_b + 2A_{ms}\Sigma_m + l\lambda \tag{S6}$$

Here, $E_{bs} = 2\kappa_m A_{ms}/R^2$ is the bending energy of the two symmetrical LD-monolayers, Σ_b and Σ_m are the ER and LD-tensions, and λ is the line tension acting along the perimeter $l = 2\pi R_{co}$ of the contact circle with radius R_{co}. $A_{bs} = L^2 - \pi R^2 \sin^2\theta$ is the area of the surrounding ER-bilayer of width L, $A_{ms} = 2\pi R^2(1-\cos\theta)$ is the surface area of the spherical monolayers with identical radii R.

Minimizing the Lagrangian $\mathcal{L}_s = F_s - \gamma V_s$ with respect to R and θ using a Lagrange multiplier γ to fulfil a constraint on fixed LD size $V_s = \pi D^3/6$, leads to a system of three equations

$$\begin{aligned}
V_s &= (2\pi/3)R^3(2+\cos\theta)(1-\cos\theta)^2 \\
\frac{\partial\mathcal{L}_s}{\partial R} &= 2\pi R^2\gamma(2+\cos\theta)(1-\cos\theta)^2 - 2\pi R\sin^2\theta\Sigma_b + 8\pi R(1-\cos\theta)\Sigma_m + 2\pi\sin\theta\lambda = 0 \\
\frac{\partial\mathcal{L}_s}{\partial\theta} &= (2\pi\gamma R^3/3)[2\sin\theta(2+\cos\theta)(1-\cos\theta) - \sin\theta(1-\cos\theta)^2] + 8\pi\kappa_m\sin\theta \\
&\quad + 4\pi R^2\sin\theta\Sigma_m - \pi R^2\sin 2\theta\Sigma_b + (2\pi R\cos\theta)\lambda = 0
\end{aligned} \tag{S7}$$

with four variables $R, \theta, \lambda, \gamma$. To solve this underdetermined system, we substituted the values of R, Σ_b, and Σ_m, obtained from the DPD simulations, into the system and solved equations (S7) for the remaining three unknowns λ, θ, and γ. The results for two LD sizes are listed in Tables S4 and S5.

S7. Membrane elasticity model for axisymmetric LDs

To determine the minimum energy shapes of symmetric lenses, we adapted a computational approach used in[5] based on the elasticity theory of fluid membranes. Here, the bottom monolayer of the lens is described as a smooth surface in terms of two parameters, the angle γ of rotation around the axis of symmetry, and the arc length s along longitudes. This surface then has Cartesian coordinates $X = R(s)\cos\gamma$, $Y = R(s)\sin\gamma$ and $Z = Z(s)$, where $0 \leq \gamma \leq 2\pi$ and $0 \leq s \leq s_1$ and R is the distance from the Z-axis, which is the axis of symmetry. We introduce a tangent angle Ψ such that $dR/ds = \cos\Psi(s)$ and $dZ/ds = \sin\Psi(s)$. In this parametrization, the volume of the lens is

$$V = 2\pi \int_0^{s_1} R^2(s)\frac{\mathrm{d}Z}{\mathrm{d}s}\mathrm{d}s \tag{S8}$$

and the total area of the two monolayers enclosing the lens is

$$A = 4\pi \int_0^{s_1} R(s)\mathrm{d}s \tag{S9}$$

The lower limit of integration, $s = 0$, corresponds to the "south pole" of the lens at which $\Psi(s = 0) = 0$, $R(s = 0) = 0$ and $Z(s = 0) = 0$. With these boundary conditions we have $R(s) = \int_0^s \cos\Psi(s')\mathrm{d}s'$ and $Z(s) = \int_0^s \sin\Psi(s')\mathrm{d}s'$. The upper limit of integration, $s = s_1$, corresponds to the lens rim, where $\Psi(s_1) = 0$ and $R(s_1) = R_1$ to connect the lens surface smoothly to a flat bilayer at a distance R_1 from the axis of symmetry. The circumference of this rim is

$$\ell = 2\pi R_1 = 2\pi \int_0^{s_1} \cos\Psi(s)\mathrm{d}s \tag{S10}$$

The energy of the system $E = E_{\mathrm{b,m}} + E_{\mathrm{b,b}} + E_{\mathrm{s,m}} + E_{\mathrm{s,b}} + E_{\mathrm{l}}$ comprises five terms: the bending energy $E_{\mathrm{b,m}}$ of the two monolayers, the bending energy of the flat bilayer, $E_{\mathrm{b,b}} = 0$, the surface energy $E_{\mathrm{s,m}}$ of the monolayers, the surface energy $E_{\mathrm{s,b}}$ of the bilayer, and the line energy E_{l} of the lens rim. Since the principal curvatures of the lens surface are given by

$C_1 = d\Psi/ds$ and $C_2 = \sin\Psi/R$ in the arc-length parametrization,[6,7] the bending energy of the two monolayers is

$$E_{\mathrm{b,m}} = 2\pi\kappa_{\mathrm{m}} \int_0^{s_1} R(s) \left(\frac{\mathrm{d}\Psi}{\mathrm{d}s} + \frac{\sin(\Psi(s))}{R(s)} - C_0 \right)^2 \mathrm{d}s \tag{S11}$$

where κ_{m} and C_0 are the bending rigidity modulus and the spontaneous curvature of the monolayers, respectively. The surface energy of the monolayers $E_{\mathrm{s,m}} = A\Sigma_{\mathrm{s}}$, where Σ_{s} denotes the surface tension of the monolayers, and the lens surface area A is given by equation (S9). The surface energy of the bilayer $E_{\mathrm{s,b}} = (L^2 - \pi R_1^2)\Sigma_{\mathrm{b}}$, where Σ_{b} denotes the surface tension of the bilayer, and L is the lateral size of the system. The energy term $L^2\Sigma_{\mathrm{b}}$ does not depend on the shape of the lens and can be omitted in numerical calculations. Finally, the line energy $E_{\mathrm{l}} = \lambda\ell = 2\pi R_1\lambda$, where λ denotes the line tension. It is convenient to use dimensionless variables in numerical calculations. Here we introduce $\tau = s/s_1$ with $\tau \in [0, 1]$, $\psi(\tau) = \Psi(s)$, $r(\tau) = R(s)/s_1$ and $z(\tau) = Z(s)/s_1$. Then, using equation (S8), s_1 can be directly related to the volume V of the lens

$$V = 2\pi s_1^3 \int_0^1 r^2(\tau)\sin(\psi(\tau))\mathrm{d}\tau \tag{S12}$$

In addition, with this choice of dimensionless variables, the total energy of the system can be written as $E = E_{\mathrm{b}} + E_{\mathrm{m}} + E_{\mathrm{l}}$ with

$$E_{\mathrm{b}} = E_{\mathrm{b,m}} + E_{\mathrm{b,b}} = 2\pi\kappa_{\mathrm{m}} \int_0^1 r(\tau) \left(\frac{\mathrm{d}\psi}{\mathrm{d}\tau} + \frac{\sin(\psi(\tau))}{r(\tau)} - C_0 s_1 \right)^2 \mathrm{d}\tau \tag{S13}$$

$$E_{\mathrm{s}} = E_{\mathrm{s,m}} + E_{\mathrm{s,b}} = 2\pi s_1^2 \left(2\Sigma_{\mathrm{m}} \int_0^1 r(\tau)\mathrm{d}\tau - \frac{1}{2}\Sigma_{\mathrm{b}} \int_0^1 \cos(\psi(\tau))\mathrm{d}\tau \right) \tag{S14}$$

and

$$E_{\mathrm{l}} = 2\pi s_1\lambda \int_0^1 \cos(\psi(\tau))\mathrm{d}\tau \tag{S15}$$

In equations (S13), (S14) and (S15), parameters $\kappa_{\rm m}$, C_0, $\Sigma_{\rm m}$, $\Sigma_{\rm b}$, and λ characterize the mechanical properties of the system whereas s_1 is determined by the volume V of the lens *via* equation (S12). Since $r(\tau)$ and $z(\tau)$ are given by $\psi(\tau)$ *via*

$$r(\tau) = \int_0^\tau \cos\psi(\tau')\mathrm{d}\tau' \tag{S16}$$

and

$$z(\tau) = \int_0^\tau \sin\psi(\tau')\mathrm{d}\tau' \tag{S17}$$

the shape of the lens is entirely determined by the function $\psi(\tau)$, and the total energy $E = E_{\rm b} + E_{\rm m} + E_{\rm l}$ is a functional of $\psi(\tau)$.

To minimize the total energy E with respect to the lens shape, as given by the function $\psi(\tau)$, it is convenient to approximate $\psi(\tau)$ by a Fourier series[8,9]

$$\psi(\tau) = \sum_{n=1}^{N} a_n \sin(n\pi\tau) \tag{S18}$$

that fulfils the boundary conditions $\psi(\tau = 0) = 0$ and $\psi(\tau = 1) = 0$. Here, N is the number of Fourier amplitudes a_n. The total energy $E = E_{\rm b} + E_{\rm m} + E_{\rm l}$, as given by equations (S13), (S14) and (S15), becomes now a function of N variables $\{a_n\}$.

We minimized E with respect to the set of Fourier amplitudes $\{a_n\}$ using a simulated annealing method. We performed the numerical calculations with $N = 100$ Fourier modes as in.[8,9] We assumed $C_0 = 0$ whereas the values of parameters $\kappa_{\rm m}$, $\Sigma_{\rm m}$, $\Sigma_{\rm b}$, λ and V were taken from the optimal fits of the spherical cup model to the lens shapes obtained in the DPD simulations. The resulting membrane profiles $\psi = \psi(s)$ are shown in Figure 3 by yellow curves juxtaposed on DPD simulation snapshots for different LD lenses.

S8. LD budding by lipid exchange

Starting from an almost spherical LD of size $D = 29.5$ nm, we created an asymmetric lipid number at constant N_{lip} (see Table S6) by exchanging lipids from the luminal to the cytosolic LD-monolayer. The resulting LDs with a given Δ were then equilibrated for 2 μs in the NPT ensemble at constant pressure 190.4×10^9 mN/m^2 using a Berendsen barostat in the vertical direction. The equilibration was followed by a 6 μs-long NVT simulation during the last 4 μs of which membrane properties were averaged over 80 simulation frames. Supplementary Table S6 lists the LD parameters for the resulting LDs shown in Fig. 4a with different cytosolic angles θ_c.

S9. Size-dependent LD-tension

Figure 2c shows ER and LD-tensions as a function of θ for an LD of size $D = 29.5$ nm. To estimate finite size effect on the LD-tensions, we repeated the same calculations for a smaller LDs of size $D = 20.3$ nm and 27.7 nm. Although LD-tensions inside spherical LDs seem to be smaller for the larger LD, see supplementary Fig. S5, their values are within the errorbars of one another. Therefore, we simulated more LDs with different sizes, four of which were used to explore size-dependent behavior of LD-tensions as shown in Fig. 6a. Supplementary Table S7 lists LD parameters for these four LDs which spontaneously formed from initial slabs.

Supplementary Figures

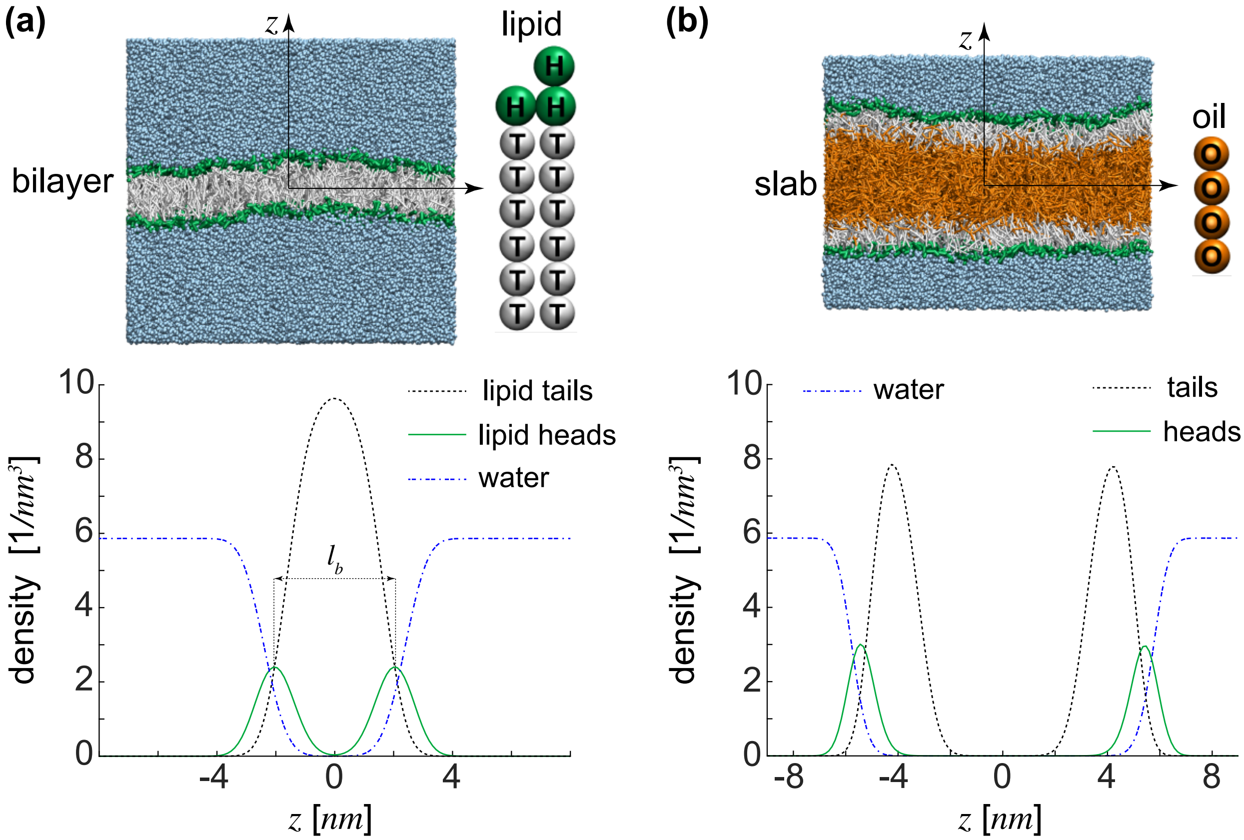

Figure S1: Coarse-grained membrane and neutral lipids with their densities: (a) A lipid bilayer with the corresponding density profiles of lipid heads, lipid tails, and water beads. The distance between the peaks of the lipid heads density defines the bilayer thickness l_b. Also shown is the structure of a lipid with its head H and tail T beads. (b) The density profiles of lipid tails and heads, and water for a slab of size $D = 24.2\ nm$. As expected water has a density of $3/d^3 = 5.86/nm^3$. Also shown is an oil molecule with its oil beads O.

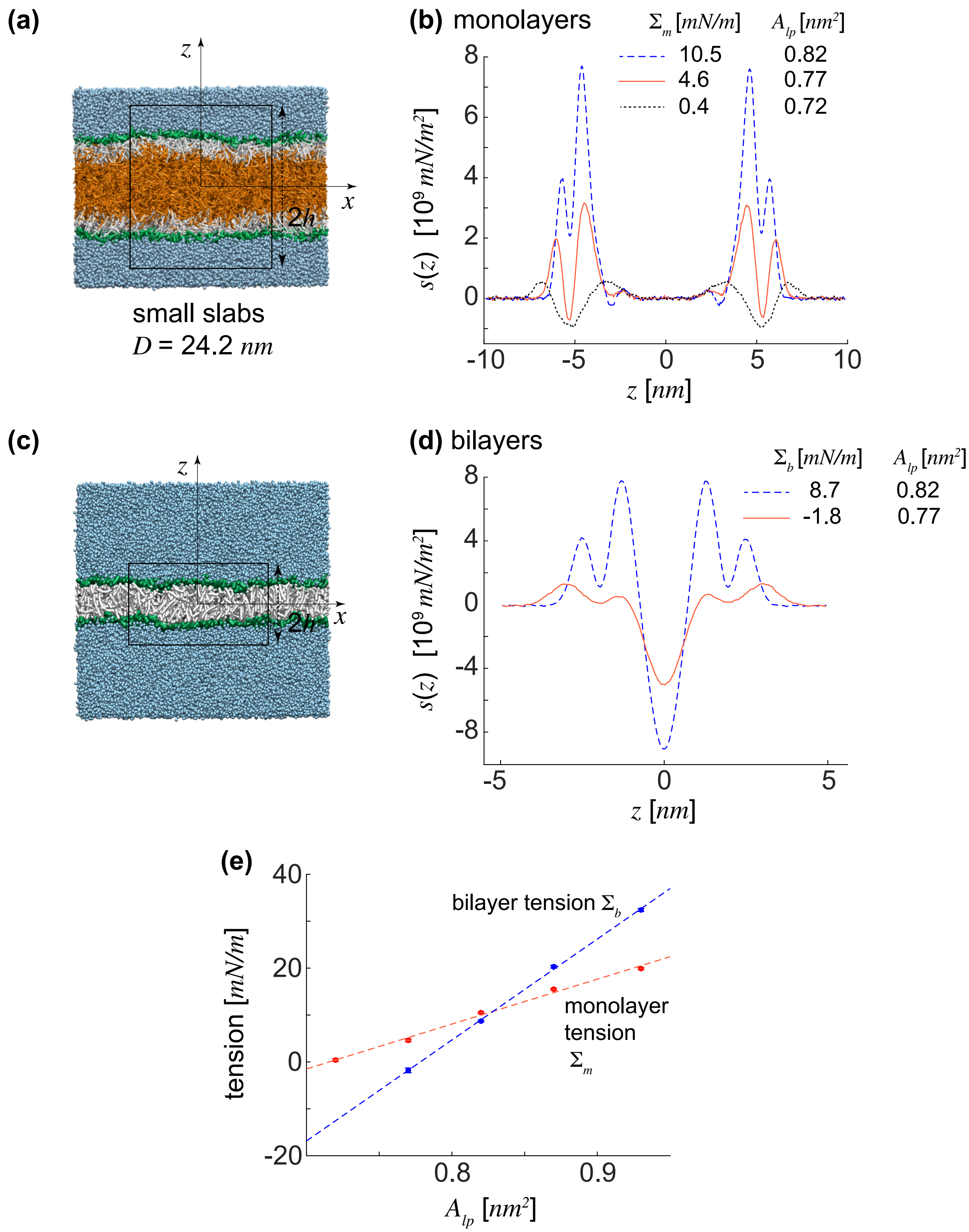

Figure S2: Finding membrane stiffness and thickness: (a) Small slabs of size $D = 24.2$ nm used to compute bending stiffness and membrane thickness of LD-monolayers with boxes of height $2h = 20$ nm and width 13 nm for calculating stress profiles as shown in (b) for three slabs. (c) Small flat bilayers with boxes of height $2h = 10$ nm and width 13 nm for calculating stress profiles in bilayers as shown in (d) for two bilayers. (e) Monolayer and bilayer tensions, Σ_m and Σ_b, plotted against A_{lp} with red and blue dots. The dashed lines, fitted to the data, were used to calculate membrane stiffness.

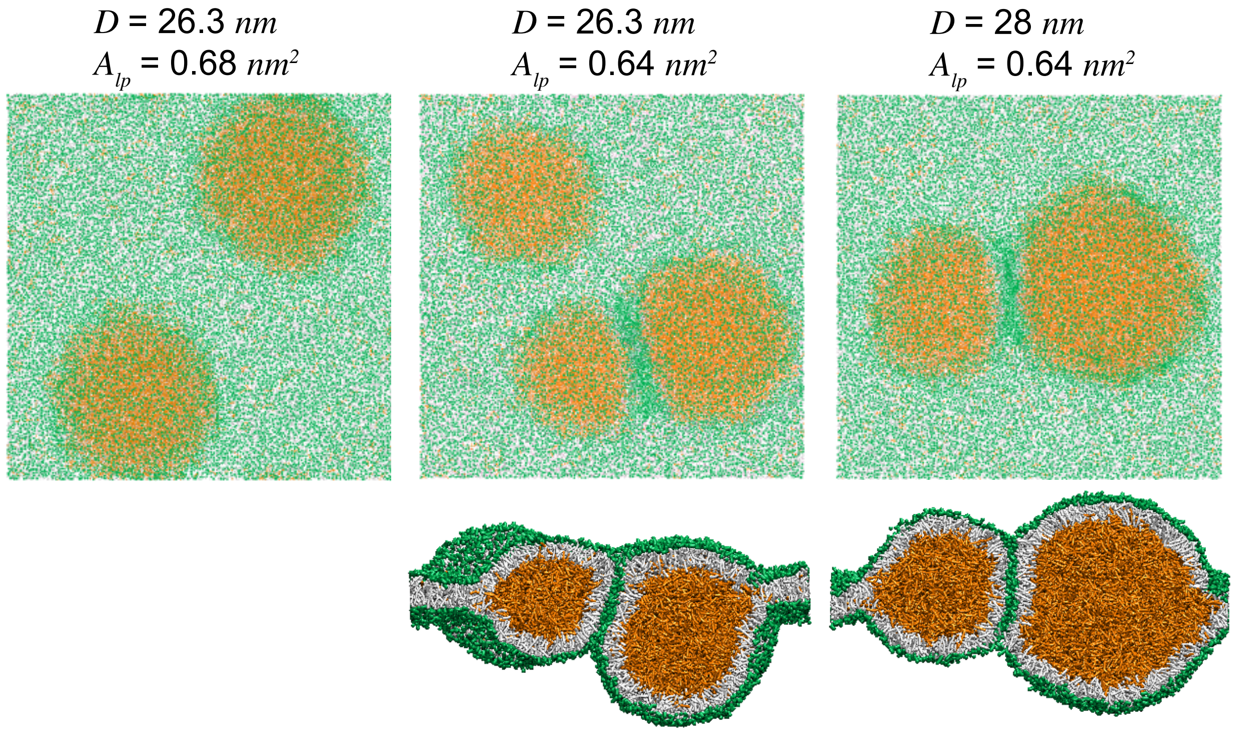

Figure S3: Multi-spherical LDs: In addition to single spherical LDs, multi-spherical LDs of smaller sizes form for sufficiently small area-per-lipids of initial slabs. Green and orange dots represent oil and lipid molecules, respectively. The bottom snapshots of the middle and right panels show the lateral cross sections of double LD structures.

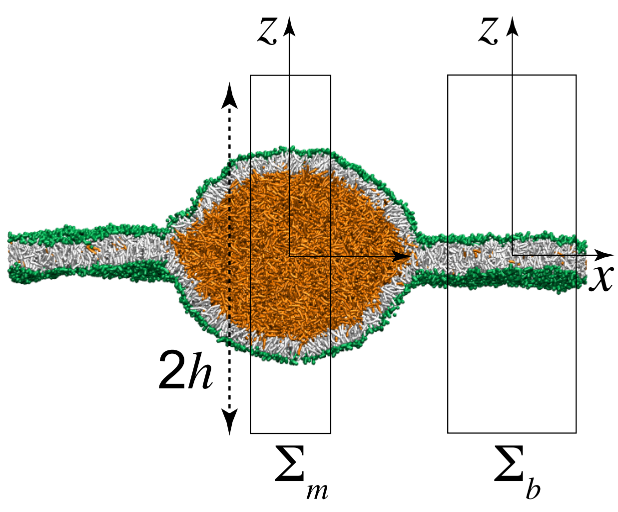

Figure S4: Stress calculation boxes: Boxes of width 5 and 8 nm and height 48 nm used to compute LD and ER-tensions, Σ_m and Σ_b, and their areas-per-lipid.

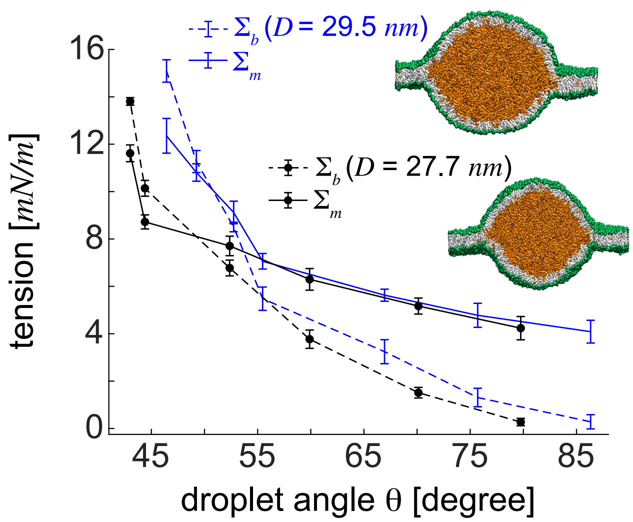

Figure S5: Size-dependent behaviour of ER and LD-tensions: ER and LD-tensions versus lens angle θ for two LDs of sizes $D = 29.5$ and $D = 27.7$ nm. LD-tensions of almost spherical LDs seem to be almost invariable for the two LD sizes.

Supplementary Tables

Table S1: DPD Interaction force parameters f_{ij} $[k_BT/d]$

	$j = W$	$j = H$	$j = T$	$j = O$
$i = W$	25	30	75	75
$i = H$	30	30	50	50
$i = T$	75	50	10	11
$i = O$	75	50	11	10

The interaction force parameter f_{ij} between oil O, water W, lipid head H, and lipid tail T beads.

Table S2: Properties of small slabs and flat bilayers

N_{lip}	A_l^m, A_l^b $[nm^2]$	Σ_m $[mN/m]$	Σ_b $[mN/m]$
1800	0.72	0.4 ± 0.6	$-$
1700	0.77	4.6 ± 0.3	-1.8 ± 0.5
1600	0.82	10.5 ± 0.2	8.7 ± 0.2
1500	0.87	15.5 ± 0.2	20.3 ± 0.3
1400	0.93	19.9 ± 0.2	32.4 ± 0.3

Areas-per-lipid and tensions of flat bilayers and small slabs of size $D = 24.2$ nm (Σ_b and Σ_m respectively) used to find the bending stiffness and membrane thickness of the ER-bilayer and LD-monolayers. All slabs contain the oil volume $V = 4264.6$ nm^3 with slab area $A_s = 655.4$ nm^2 and minimum slab area $A_{sm} = 1115.3$ nm^2. The monolayer thickness is $l_m = 2.04$ nm.

Table S3: Properties of initial slabs used for identifying relevant LD parameters

N_{oil}	D $[nm]$	V $[nm^3]$	N_{lip}	A_{lp} $[nm^2]$	A_{sm} $[nm^2]$
21000	29.5	8601.6	6800	0.68	2987.5
			6400	0.72	
			6000	0.77	
			5600	0.822	
24881	31	10192	7200	0.64	3058.8
			6428	0.716	
			5625	0.819	
31500	33.2	10902.4	6800	0.68	3169.7
			6400	0.72	
			6000	0.77	

Properties of slabs with different sizes used for spontaneous formation of LDs and identifying LD parameters. The data corresponds to slabs the resulting LDs of which are shown in Figure 1c. The slab area is $A_s = 2304$ nm^2 and the monolayer thickness is $l_m = 2.04$ nm for all slabs.

Table S4: Properties of symmetrical LD lenses with size $D = 29.5$ nm

L $[nm]$	R $[nm]$	θ $[°]$	Σ_b $[mN/m]$	Σ_m $[mN/m]$	λ $[pN]$	γ $[10^9$ $mN/m^2]$
47.2	14.2 ± 0.3	86.3 ± 0.1	0.3 ± 0.3	4.1 ± 0.5	10 ± 4.4	-0.615
48	15.9 ± 0.3	75.7 ± 0.07	1.3 ± 0.4	4.8 ± 0.5	-3.4 ± 7.2	-0.641
48.8	18 ± 0.4	67 ± 0.04	3.2 ± 0.5	5.6 ± 0.2	-8.4 ± 8.7	-0.659
49.6	21.9 ± 0.3	55.6 ± 0.03	5.5 ± 0.5	7.1 ± 0.3	-36.1 ± 10.9	-0.68
50.4	23.3 ± 0.3	52.7 ± 0.03	8.5 ± 0.2	9.1 ± 0.5	-38.2 ± 11.8	-0.811
51.2	25.2 ± 0.3	49.2 ± 0.03	11.3 ± 0.5	10.8 ± 0.4	-45.7 ± 13.8	-0.885
52	27 ± 0.5	46.4 ± 0.03	15.5 ± 0.1	11.7 ± 0.4	-31.1 ± 21	-0.892

Properties of LD lenses obtained by increasing the width L of the simulation box of an almost spherical LD of size $D = 29.5$ nm with smallest box width $L = 47.2$ nm.

Table S5: Properties of symmetrical LD lenses with size $D = 27.7$ nm

L $[nm]$	R $[nm]$	θ $[°]$	Σ_b $[mN/m]$	Σ_m $[mN/m]$	λ $[pN]$	γ $[10^9$ $mN/m^2]$
48	14.1 ± 0.4	79.7 ± 0.1	0.27 ± 0.15	4.2 ± 0.5	-2.8 ± 3.3	-0.901
48.8	15.9 ± 0.3	70.1 ± 0.06	1.5 ± 0.2	5.2 ± 0.3	-17.2 ± 4.3	-0.702
49.6	18.8 ± 0.6	59.9 ± 0.04	3.8 ± 0.4	6.3 ± 0.5	-30.3 ± 10.6	-0.713
50.4	21.8 ± 0.5	52.4 ± 0.04	6.8 ± 0.3	7.7 ± 0.4	-35.9 ± 10	-0.744
51.2	26.5 ± 0.7	44.4 ± 0.03	10.1 ± 0.3	8.7 ± 0.3	-36.6 ± 9.8	-0.687
52	27.5 ± 0.4	43 ± 0.03	13.8 ± 0.2	11.6 ± 0.4	-52.9 ± 11.6	-0.873

Properties of LD lenses obtained by increasing the width L of the simulation box of an almost spherical LD of size $D = 27.7$ nm with the smallest box width $L = 48$ nm.

Table S6: Properties of asymmetric LDs budding to the cytosol

N_{cm} N_{lm}	θ_c [°]	Σ_b $[mN/m]$	Σ_{cm} $[mN/m]$ Σ_{lm} $[mN/m]$	Δ
7000 7000	91.6 ± 1	0.073 ± 0.16	3.85 ± 0.39 4.8 ± 0.7	0
7150 6850	101.3 ± 3.3	-0.19 ± 0.23	4.7 ± 1.1 4 ± 1.1	0.021
7300 6700	108.9 ± 2.4	0.05 ± 0.34	4.7 ± 0.4 4.9 ± 0.7	0.043
7450 6550	115.8 ± 1.3	-0.21 ± 0.24	3.9 ± 0.6 4.6 ± 0.6	0.064
7600 6400	126.4 ± 3.3	-0.075 ± 0.26	4.3 ± 1 4.2 ± 1.2	0.086
7750 6250	133.3 ± 2.6	-0.033 ± 0.25	4.3 ± 0.9 4.1 ± 1	0.107
7900 6100	142.4 ± 2.3	-0.018 ± 0.27	4.7 ± 0.7 3.9 ± 0.6	0.129
8050 5950	148.4 ± 1.9	0.037 ± 0.2	4.1 ± 1 5.1 ± 0.5	0.15
8200 5800	163.4 ± 2.4	-0.064 ± 0.22	4.3 ± 0.6 4.3 ± 0.8	0.171

Properties of spherical LDs obtained by exchanging lipids from the luminal to the cytosolic monolayer of an initial spherical LD of size $D = 29.5$ nm in a fixed simulation box of width $L = 72$ nm. The initial spherical LD emerges into a completely budded LD attached to the ER upon exchanging lipids at a fixed total number of lipids $N_{lip} = 14000$. N_{cm} and N_{lm} denote number of lipids in the cytosolic and luminal leaflets of the LD-monolayers and the ER bilayer. LD angles are calculated based on the LD budding model (Fig. 5b) with $\theta_l = 180 - \theta_c$.

Table S7: Properties of almost spherical LDs with different sizes

N_{oil}	D $[nm]$	N_{lip}	A_{lp} $[nm^2]$
5500	20.3	6400	0.76
16800	27.7	6800	0.68
21000	29.5	6960	0.66
31500	33.2	7200	0.64

Projected areas-per-lipid A_{lp} for three nearly-spherical LDs of different sizes.

References

1. Ghosh, R.; Satarifard, V.; Grafmueller, A.; Lipowsky, R. Spherical nanovesicles transform into a multitude of nonspherical shapes. *Nano Letters* **2019**, *19*, 7703–7711.

2. Sabet, F. K.; Bahrami, A.; Bahrami, A. H. Compartmentalizing and sculpting nanovesicles by phase-separated aqueous nanodroplets. *RSC advances* **2022**, *12*, 32035–32045.

3. Marsh, D. Elastic curvature constants of lipid monolayers and bilayers. *Chemistry and Physics of Lipids* **2006**, *144*, 146–159.

4. Satarifard, V.; Grafmueller, A.; Lipowsky, R. Nanodroplets at membranes create tight-lipped membrane necks via negative line tension. *ACS Nano* **2018**, *12*, 12424–12435.

5. Różycki, B.; Boura, E.; Hurley, J. H.; Hummer, G. Membrane-elasticity model of Coatless vesicle budding induced by ESCRT complexes. *PLOS Computational Biology* **2012**, *8*, e1002736.

6. Jülicher, F.; Seifert, U. Shape equations for axisymmetric vesicles: a clarification. *Physical Review E* **1994**, *49*, 4728–4731.

7. Jülicher, F.; Lipowsky, R. Shape transformations of vesicles with intramembrane domains. *Physical Review E* **1996**, *53*, 2670–2683.

8. Góźdź, W. Influence of spontaneous curvature and microtubules on the conformations of lipid vesicles. *Journal of Physical Chemistry B* **2005**, *109*, 21145–21149.

9. Góźdź, W. Deformations of lipid vesicles induced by attached spherical particles. *Langmuir* **2007**, *23*, 5665–5669.